International Journal of Astrophysics and Space Science
2024, Vol. 12, No. 1, pp. 1-16
https://doi.org/10.11648/j.ijass.20241201.11

Research Article

Variability of Ionospheric Total Electron Content Over Morocco During the Godzilla Sand and Dust Storm of June 2020

Uluma Edward[1, *], Chali Idosa Uga[2, 5], Athwart Davis Odhiambo[1], Binod Adhikari[3], Sujan Prasad Gautam[5], Ndinya Boniface[1], Omondi George[4], Ashutosh Giri[3], Dessalegn Teferi[2], Negasa Belay[2], Ashok Silwal[5]

[1]Department of Physics, Masinde Muliro University of Science & Technology, Kakamega, Kenya
[2]Department of Physics, Jimma University, Jimma, Oromia, Ethiopia
[3]Department of Physics, St. Xaviers's College, Kathmandu, Nepal
[4]Department of Physics and Materials Science, Maseno University, Maseno, Kenya
[5]Department of Space Science, University of Alabama in Huntsville, Alabama, USA

Abstract

During sand and dust storm (SDS) events, atmospheric suspension and transport of sand and dust brings a reasonable amount of electrification in the atmosphere which plays a very important role in the atmosphere-ionosphere coupling. The Godzilla SDS began on 5th June 2020 in Algeria following a decrease in pressure and spread to other areas across the Sahara between 6th and 28th June 2020. Using SDS data from Copernicus Sentinel-5P satellite mission and Vertical Total Electron Content (VTEC) data from four GNSS receiver stations: IFR1 (Ifrane Seismic), MELI (Melilla), TETN (Tetouan) and OUCA (Ouca) over Morocco, we investigate the possible ionospheric TEC variability over the four GNSS receiver stations during the Godzilla SDS event which was tracked using the Sentinel-5P Satellite mission. Solar wind parameters: Horizontal component of Interplanetary Magnetic Field (IMF-Bz), interplanetary Electric Field (IEF-Ey) and solar wind speed (V) and geomagnetic indices: Disturbance Storm Time (Dst) and Planetary K (Kp) indices were examined and showed very minimal geomagnetic influence during the period. We observed major ionospheric disturbances over the four Global Navigation Satellite System (GNSS) receiver stations on 16th, 17th, 18th, 21st, 22nd, 23rd 25th and 26th June 2020: the period with the Sentinel-5P Aerosol Index (SAI) of more than 4 as recorded by the Sentinel-5P Satellite engine. The daily VTEC values over the four GNSS receiver stations recorded continuous electron density perturbations during these days. Apart from the ionospheric TEC perturbations, significant enhancements and decreases in daily maximum VTEC values over the four GNSS receiver stations were also noted. These were attributed to the changes in the atmospheric electric fields generated by the SDS event. The VTEC plots for each day exhibited similar trends, hence exhibited the same ionospheric dynamics. VTEC depletions of depths 3 to 6 TECU over all the four GNSS receiver stations were noted on 12th, 14th, 17th, 20th and 25th June 2020. Nighttime VTEC enhancements were also noted and majorly occurred between 20:00 and 21:00 UT on 9th, 13th, 15th, 17th, 19th, 20th and 21st June 2020. This was attributed to the development of the electron avalanche processes including dust and electron absorption or losses and the active conversion to electron dissociative attachment leading to electron excitation. In conclusion, the Godzilla SDS of June 2020 led to the electron density

*Corresponding author: nyogesa_edward@yahoo.com (Uluma Edward)

Received: 2 May 2024; **Accepted:** 22 May 2024; **Published:** 15 July 2024

perturbations over Morocco.

Keywords

Godzilla Sand and Dust Storm, Atmospheric Electric Fields, Aerosols, Vertical Total Electron Content

1. Introduction

A sand and dust storm (SDS) is a meteorological phenomenon that commonly occurs in arid and semi-arid regions. It occurs when loose sand and dust are blown over long distances from one region to another [1]. Between 5th and 28th June 2020, the Earth experienced a very thick and dense dust plume travelling over 5000 miles along the African Saharan desert towards the United States (USA) and the Caribbean and having a greater wind velocity compared to others that have ever occurred [2]. The dust storm was nicknamed 'Godzilla' due its intense impact and gravity [3, 4]. According to National Oceanic and Atmospheric Administration (NOAA), the Godzilla SDS is approximated to be between 60% to 70% larger than the dust storms experienced in the past [5]. The uprising of the Godzilla SDS took place on 5th June 2020 in Algeria following a decrease in pressure [4] and spread to other areas across the Sahara between 6th and 28th June 2020. The background cause of this particular event still remains unclear with some hypothesis pointing at extra Earth warming which degenerated into extreme convectional currents or it being a meteorological anomaly [6].

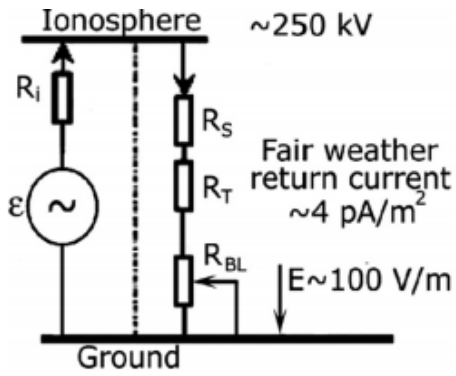

Figure 1. *Model diagram of the Global Electric Circuit (GEC) [13, 14].*

The ionosphere varies with latitude, longitude, altitude, season, universal time and geomagnetic activity [7-9]. This ionospheric variability arises from time delays, atmosphere-ionosphere couplings and other magnetospheric, interplanetary and mesospheric processes and variations in electric fields and neutral composition [10]. During SDS events, atmospheric suspension and transport of sand and dust brings a reasonable amount of electrification in the atmosphere with an electric field of between 10Kv/m and 100Kv/m being observed in the terrestrial atmosphere [11]. This electrification process plays a very important role in the atmosphere-ionosphere coupling during the period [12]. Sand and dust particles flowing in the atmosphere during SDS usually modify the electric properties of the lower atmosphere, leading to creation of low conducting layers (caused by the ion-aerosol attachment) which increases column resistance for the vertical current flowing between the upper conducting layer (ionosphere) and the ground within the Global Electric Circuit (GEC) model indicated in Figure 1.

In the model diagram of the GEC, Ɛ; R_i; R_S; R_T and R_{BL} represent atmospheric electric fields, internal resistance of the atmospheric electric fields, resistance of the stratosphere, the resistance of the troposphere and the resistance of the atmospheric boundary layer respectively. The average potential difference at the ionosphere is about 250 kV while the average electric field gradient on the Earth's surface is about 100V/m, with the potential difference between the ionosphere and the Earth's surface ranging between 150 and 500 kV [13]. The electrical conductivity of the atmosphere provides information on the ionization processes that controls the electrical state of the atmosphere and on the major charged particle species, free electrons, positive and negative ions that are present in the medium according to the GEC [11]. The upper atmosphere has a higher conductivity than the lower atmosphere as a result of ionization from highly varying and energetic background source of energetic particles that bombard the Earth continuously (galactic cosmic rays) [18]. Conductivity of the upper atmosphere arises from presence of free electrons and ions which can readily move under impressed forces and thus act as efficient charge carriers. The electrons and ions respond differently to the impressed forces such that ion and electron currents are necessarily not the same [15]. In cases where the positive and negative particles move in the opposite directions, the electrons and ions are added together but in cases where the ions and electrons move exactly together, the two currents usually cancel out, hence no net current. However, in any of the two cases, the plasma as a whole is in motion, in what is known as plasma drift [15]. Hoppel, W. A. et al, have shown that the atmospheric boundary layer is about 75% of the total resistance of the atmospheric column between the lower ionosphere and the Earth's surface [16]. Hence, the presence of aerosols in the atmosphere during SDS events increases the resistance of the atmospheric boundary layer [17], leading to an increase in

potential drop on the boundary layer. This results in the growth of the ionosphere potential relative to the Earth's surface. Positive electron density anomalies are then formed in the ionosphere above the affected regions [13, 14, 17-19].

Pulinets, S. et al, studied the atmosphere-ionosphere coupling induced by dust storms using Differential Global Ionospheric Maps (GIM) Total Electron Content (TEC) mapping procedure to show specific features of ionospheric reaction. Their results revealed positive ionospheric phenomena over the area of air pollution and over the magnetically conjugated area in low latitude and equatorial regions. They concluded that the phenomena posed double error for precise point positioning (PPP) due to sharp TEC gradients on the borders of the formed positive irregularities of electron concentration [14]. Tramutoli, V. et al, analyzed two Saharan dust events of May 2008 which were detected by Robust Satellite Techniques (RST) using Spinning Enhanced Visible and Infrared Imager (SEVIRI) optical data. The DETEMER and GPS-TEC showed some ionospheric perturbations over the Mediterranean basin. Generally, their study confirmed the perturbing effects of dust and volcanic events on tropospheric and ionospheric parameters [20]. The atmosphere-ionosphere interactions due to SDS events are unique and quite complex as they depend on the structure of the storm and various atmospheric factors. Thus further studies needs to be done to fully understand the dynamics behind it.

Examining changes in TEC during SDS events play a critical role in unraveling possible intricate relationship between these natural occurrences and the ionosphere. Although this is an open scientific problem (an on-going research) how SDS event triggers ionospheric TEC; the possible mechanism proposed are that during these storms, various elements such as sand and dust aerosols infiltrate the atmosphere, impacting electron distribution, while charged particles alter the ionosphere's electrical properties. Furthermore, the atmospheric disturbances generated by these storms influence electron density and subsequently affect TEC measurements. In this paper, we investigate and present results on the possible ionospheric TEC variability brought about by the atmospheric-ionospheric interaction during the Godzilla SDS of June 2020 over Morocco using GPS-TEC data from four Global Navigation Satellite Systems (GNSS) receiver stations: IFR1 (Ifrane Seismic), OUCA (Ouca), MELI (Melilla) and TETN (Tetouan), all situated in Morocco. We focus our study on TEC measurement using Global Positioning Satellite (GPS) receivers as it is a reliable and cost-effective method of probing the thermosphere-ionosphere system [21].

2. Data Acquisition and Methodology

2.1. Geomagnetic Indices and Solar Wind Parameters Data

In this study we considered the period between 1st and 30th June 2020 which was the period in which the Godzilla SDS occurred over the Sahara. The geomagnetic indices data that show the level of the geomagnetic activity between 1st and 30th June 2020 were obtained using Kp index: *www.kugi.kyoto-ua.ac.jp/kp* and Dst index: *wdc.kugi.kyoto.u.ac.jp/dst/index.html.* The daily values of solar wind parameters such as interplanetary magnetic field (IMF-Bz), interplanetary electric field (IEF-Ey) and solar wind speed (V) were obtained from: *https://omniweb.gsfc.nasa.gov/form/dx1.html.*

2.2. IGS Data

In this study, the GPS-TEC data over four stations whose Geomagnetic coordinates are: IFR1 (33.51393 ℕ, 354.8748 𝔼); MELI (35.28119 ℕ, 357.048 𝔼); OUCA (31.20659 ℕ, 352.13349 𝔼) and TETN (35.56165 ℕ, 354.63699 𝔼) in Morocco was accessed from the University of NAVSTAR Consortium dual frequency devices (http://unavco.org/data/gps-gnss/data-access methods/*dai1/dai1.html*). GPS-TEC data in the IGS receivers is saved in the zipped Receiver Independent Exchange (RINEX) Format and then adapted to GPS observable files with the use of appropriate software [22]. These GPS measurements are either code pseudoranges (P) or carrier phases (ϕ). The receiver receives the code time delay and carrier phase difference by cross-correlating the f_1 and f_2 modulated carrier signals, which are normally considered to travel along the same path through the ionosphere [23]. It is acceptable to obtain estimates of GPS-derived ionospheric TEC using dual frequency GPS measurements [24, 25]. GPS receiver data are critical for estimating the electron density along a ray path between a GPS satellite and a ground receiver [26, 27]. Dual-frequency GPS receivers may offer integral information on the ionosphere and plasmasphere by computing the differential of the code and carrier phase measurements, in addition to removing ionospheric inaccuracies in TEC estimates [28, 29]. As a result, the GPS-TEC computed by the dual-frequency receivers is offered as an input to an ionosphere assimilation model [30]. For the present study, GPS data collected in dual-frequency receivers was used, and GPS-TEC data was obtained using the pseudo-range and carrier phase measurements. The TEC calculated from the pseudo-range measurement (slant TEC) is given by the following Equation 1:

$$STEC = \frac{1}{40.3}\left[\frac{f_1^2 f_2^2}{f_1^2 - f_2^2}\right](P_2 - P_1) \quad (1)$$

Similarly, the TEC from carrier phase measurement may be calculated as follows using Equation 2:

$$STEC = \frac{1}{40.3}\left[\frac{f_1^2 f_2^2}{f_1^2 - f_2^2}\right](\phi_2 - \phi_1) \quad (2)$$

where f_1 and f_2 are GPS satellite frequencies determined from the fundamental frequency, f_o=10.23MHz as: (f_1=154, f_o=1,575.42MHz), (f_2=120, f_o=1,227.60 MHz), and the differential code and phase measurements are ($P_2 - P_1$) and ($\phi_1 - \phi_2$), respectively [31]. The vertical total electron content (VTEC) is obtained using the relations in electrons per metre square using Equation 3:

$$VTEC = STEC \times Cos(\chi') \tag{3}$$

where the zenith angle χ' is given by Equation 4:

$$\chi' = \arcsin\left[\frac{R_E \cos\alpha}{R_E + h} Sin(\chi)\right] \tag{4}$$

VTEC is therefore given by equation 5:

$$VTEC = STEC\left\{\cos\left[\arcsin\left(\frac{R_E \cos\alpha}{R_E + h}\right)\sin(\chi)\right]\right\} \tag{5}$$

Where α is the satellite's elevation angle, R_E is the Earth's mean radius, and h is the height of the ionospheric layer, which is considered to be 400 km.

To reduce multipath effects, the data selected was for elevation angles of 30 °and above [32].

Information for the four GNSS receiver stations: MELI, IFR1, OUCA and TETN is given in Table 1:

Table 1. *Information of the geographical and geomagnetic locations of the stations over Morocco.*

Station ID	Station Name	Geographic Latitude	Geographic Longitude	Geomagnetic Latitude	Geomagnetic Longitude	Local Time
MELI	Melilla	35.28 ℕ	-2.95 ℍ	26.67 ℕ	73.64 ℍ	UT-1
IFR1	Ifrane Seismic	33.52 ℕ	-5.13 ℍ	24.23 ℕ	71.59 ℍ	UT-1
OUCA	Ouca	31.206 ℕ	-7.87 ℍ	21.09 ℕ	69.02 ℍ	UT-1
TETN	Tetouan	35.56 ℕ	-5.36 ℍ	27.35 ℕ	71.78 ℍ	UT-1

The average daily data of VTEC for all PRNs for IFR1, MELI, OUCA and TETN for all the days between 1st and 28th June 2020 were obtained by averaging the VTEC values for all identical pseudo-random numbers (PRNs) within a 24 hour period [33] and used to plot VTEC against Universal Time (UT) for each day and station. The VTEC against UT plots for each day were analyzed.

3. Results

3.1. Movement of the June 2020 Godzilla SDS over the Sahara

The movement of the Godzilla SDS over the Sahara was tracked using the Copernicus Sentinel-5P satellite mission which was launched by the European Space Agency (ESA) on 13th October 2017. This satellite tracked the movement of the Godzilla SDS from 1st June to 30th June 2020 across the Sahara desert using the Google Earth Engine (GEE), which is a cloud-based platform that stores a variety of satellite images used to detect changes in landscape [34] and the Sentinel-5P Aerosol Index (SAI), which qualitatively shows elevated aerosol layers in atmosphere [35]. Between 1st and 3rd June 2020, the Godzilla SDS was observed in Niger, Mali and Chad as in Figure 2(a), 2(b) and 2(c). Between 4th and 6th June 2020, the dust plume was seen to expand horizontally covering a wider range towards Mauritania as in Figure 2(d), 2(e) and 2(f). By 7th to 9th June 2020, the Godzilla SDS had extended to Western Sahara, Niger, Mauritania, Chad [36, 37] as in Figure 2(g), 2(h), and 3(a). Between 10th and 12th June 2020, the dust plume extended to eastern countries such as Libya and Sudan as in Figure 3(b), 3(c) and 3(d). Between 15th and 18th June 2020, the Western part of Africa such as Mauritania, Mali, Morocco and Western Sahara felt the greatest impact of the Godzilla SDS [6] as in Figure 3(g), 3(h), 4(a) and 4(b). By 20th June 2020, the first traces of dust had reached the Caribbean [38] as in Figure 4(d) and 4(e).

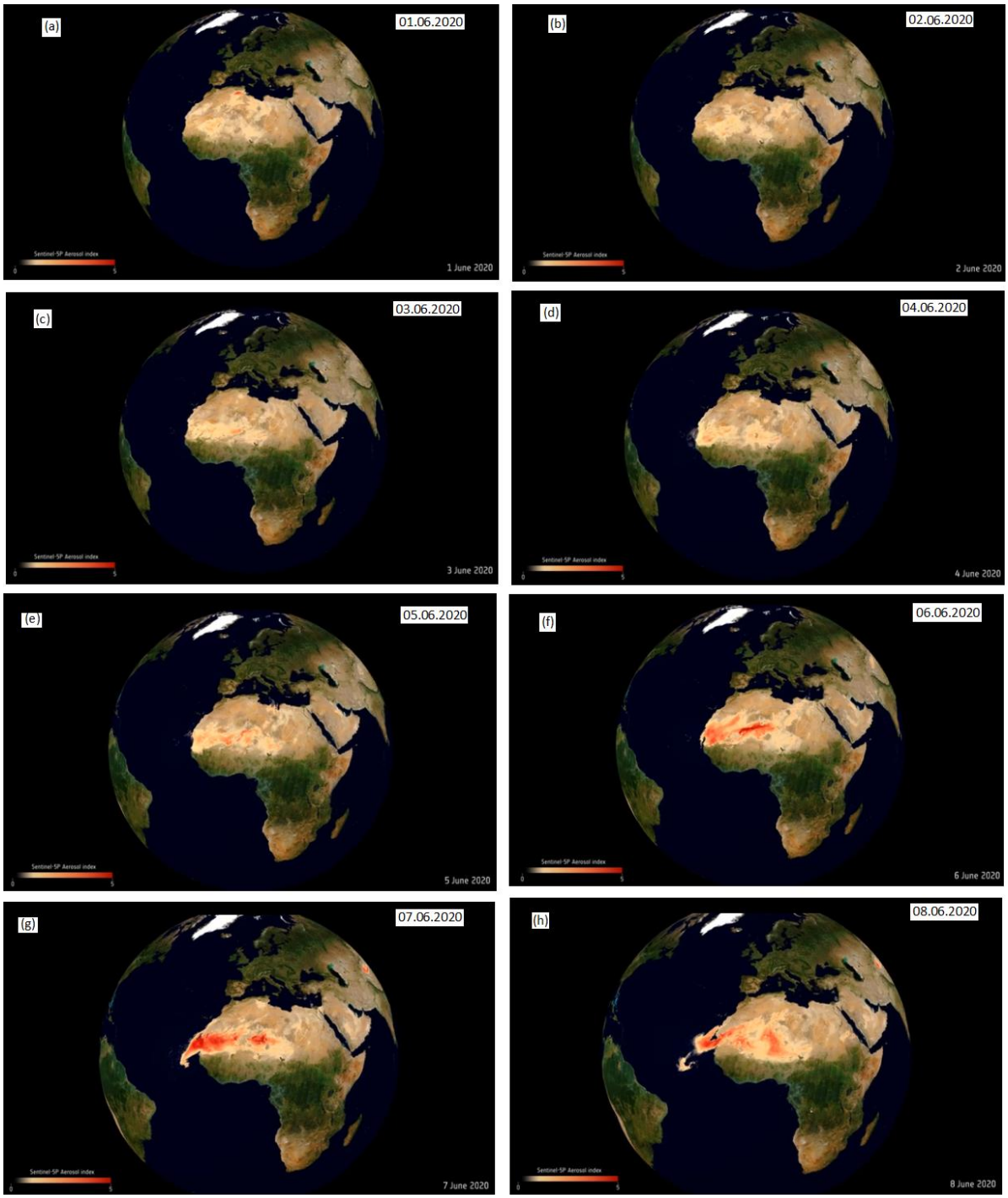

Figure 2. *The Copernicus Sentinel-5P satellite images of Godzilla SDS over the Sahara for (a 01.06.2020 (b) 02.06.2020 (c) 03.06.2020 (d) 04.06.2020 (e) 05.06.2020 (f) 06.06.2020 (g) 07.06.2020 and (h) 07.06.2020 (Modified Copernicus Sentinel data, 2020, processed by ESA).*

From 21st June to 26th June 2020, large SDS traces moved to the upper parts of the Sahara as in Figures 4(e), 4(f), 4(g), 4(h), 5(a) and 5(b). Between 28th and 30th June 2020, there was a decrease in the dust plume crossing over into the Atlantic Ocean.

In Figures 2, 3, 4 and 5, the cream colour on the SAI indicates absence of aerosol in the atmosphere while red colour shows presence of aerosols in high concentrations during the Godzilla sand and dust storm of June 2020 as tracked by the Copernicus Sentinel-5P satellite.

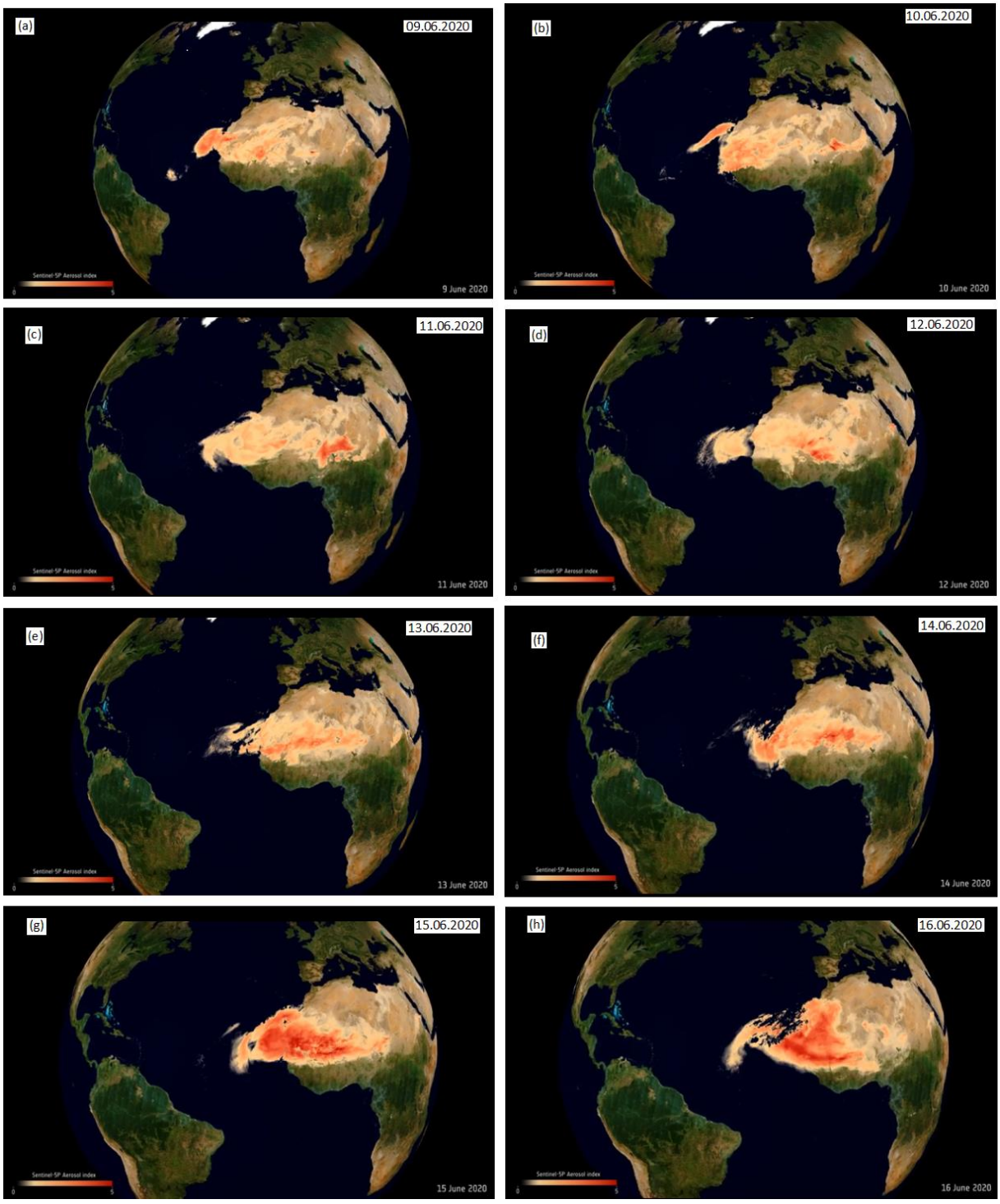

Figure 3. *The Copernicus Sentinel-5P satellite images of Godzilla SDS over the Sahara for (a) 09.06.2020 (b) 10.06.2020 (c) 11.06.2020 (d) 12.06.2020 (e) 13.06.2020 (f) 14.06.2020 (g) 15.06.2020 and (h) 16.06.2020 (Modified Copernicus Sentinel data, 2020, processed by ESA).*

A close analysis of the Copernicus Sentinel-5P satellite images from 1st June to 26th June 2020 shows a noticeable change in the aerosol concentrations over the Sahara during the period. The greatest influence of the Godzilla SDS over Morocco was felt between 16th and 26th June 2020 as depicted by Figures 3(h), 4(a), 4(b), 4(c), 4(d), 4(e), 4(f), 4(g), 5(a) and 5(b).

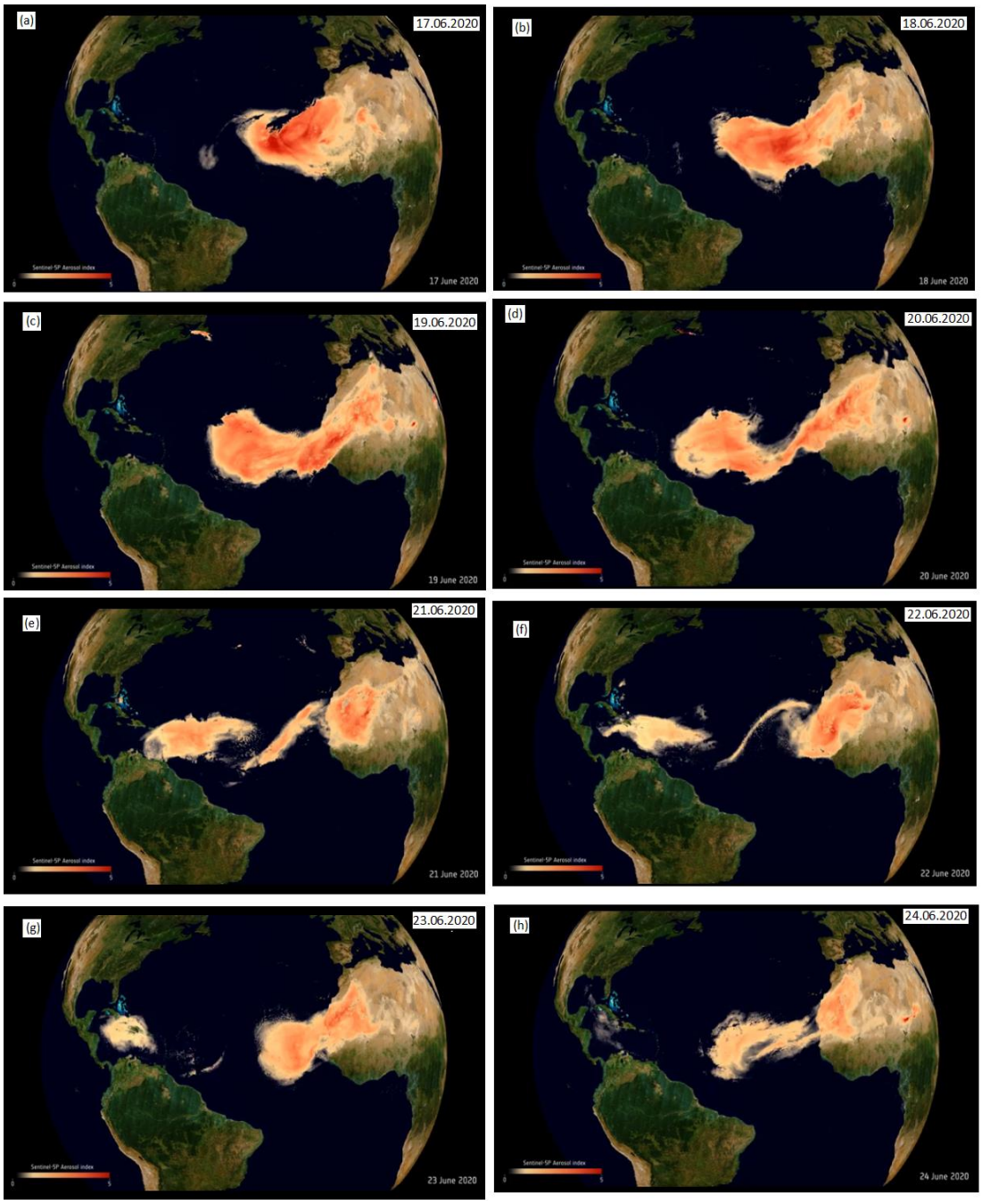

Figure 4. *The Copernicus Sentinel-5P satellite images of Godzilla SDS over the Sahara for (a) 17.06.2020 (b) 18.06.2020 (c) 19.06.2020 (d) 20.06.2020 (e) 21.06.2020 (f) 22.06.2020 (g) 23.06.2020 and (h) 24.06.202 (Modified Copernicus Sentinel data, 2020, processed by ESA).*

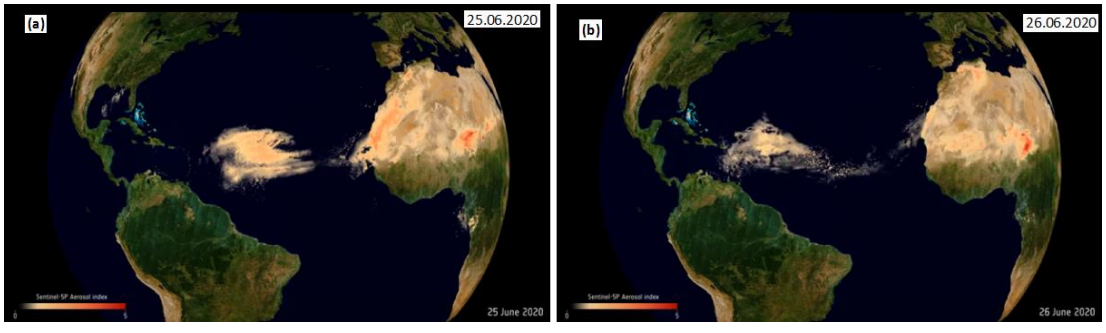

Figure 5. *The Copernicus Sentinel-5P satellite images of Godzilla SDS over the Sahara for (a) 25.06.2020 and (b) 26.06.202 (Modified Copernicus Sentinel data, 2020, processed by ESA).*

3.2. Variation of Solar Wind Parameters Between 1st and 30th June 2020

Figure 6 depicts the changes in IMF-Bz, IEF-Ey, V, K_p and Dst indices between 1st and 30th June 2020.

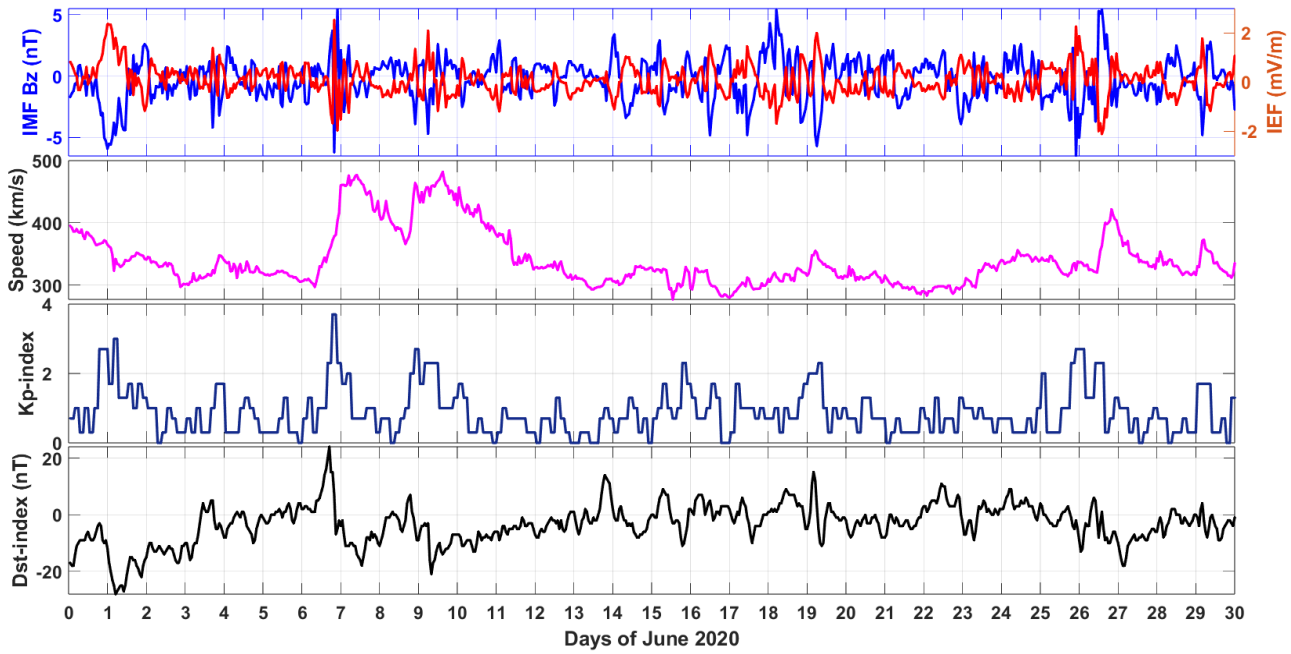

Figure 6. *Variations of Solar wind parameters: IMF-Bz, IEF-Ey and V speed and the geomagnetic indices: K_p and Dst index, between 1st and 30th June 2020.*

From Figure 6 it is noted that the least value of the southward turning of the IMF-Bz was -6 nT with corresponding rise of IEF-Ey of 4 mV/m on 1st June, 7th June, 19th June and 26th June 2020. The solar wind speed rose to maximum of about 470 km/s on 7th and 10th June 2020. The highest kp index value of about 3.7 was attained on 7th June 2020. The lowest Dst value of -25 nT was attained on 1st June 2020. The solar wind parameters in Figure 6 show a minimum solar wind speed of 270 km/s on 16th June 2020 and maximum solar wind of 360 km/s on 20th June 2020. Generally, between 1st and 30th June 2020, IMF-Bz ranged between -6 and 5nT while IE-Ey ranged between -3 and 3 mV/m. The V ranged between 300 and 470km/s. The Kp index values ranged between 0 and 3.7 while the Dst index ranged between -30 and 20 nT. In summary, the values of the solar wind parameters and geomagnetic indices between 1st and 30th June 2020 in Figure 6 indicate that the geomagnetic field influence on the ionosphere was very minimal during the study period.

3.3. Variations of VTEC Against Universal Time (UT) During the Godzilla SDS of June 2020 over IFR1, MELI, OUCA and TETN

The ionospheric variability over IFR1, MELI, OUCA and TETN in Morocco was examined using VTEC against UT plots for the period between 1st and 28th June 2020.

3.3.1. Variations of VTEC Against UT Between 1st and 4th June over IFR1, MELI, OUCA and TETN

Figure 7(a), 7(b), 7(c) and 7(d) shows VTEC against UT plots over IFR1, MELI, OUCA and TETN on 1st, 2nd, 3rd and 4th June 2020 respectively. There was a noticeable reduction in daily maximum VTEC values over all the four GNSS receiver stations between 1st and 4th June 2020. IFR1 had a daily maximum VTEC value of 14 TECU on 1st June, which reduced to 13 TECU on 2nd and 3rd June 2020 and to 12 TECU on 4th June 2020. MELI had a daily maximum VTEC value of 17 TECU on 1st June, which reduced to 16 TECU on 2nd June, 15 TECU on 3rd June and 12 TECU on 4th June 2020. OUCA had a daily maximum VTEC value of 19 TECU on 1st June, which reduced to 17 TECU on 2nd and 3rd June and 14 TECU on 4th June 2020. TETN had a daily maximum VTEC value of 17 TEC on 1st and 2nd June, which reduced to 14 TECU on 3rd June and 13 TECU on 4th June 2020. TEC depletions of depth between 3 – 4 TECU were also observed between 12:00 UT and 18:00 UT over IFR1 and OUCA on 2nd June and over IFR1, MELI, OUCA and TETN on 4th June 2020.

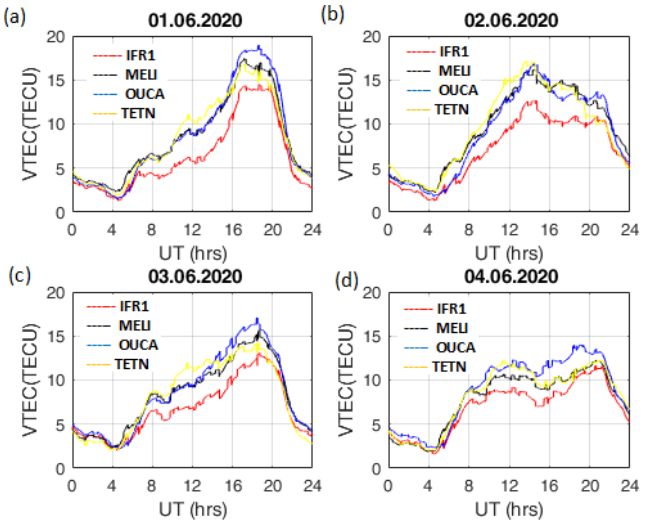

Figure 7. *Plot of VTEC against UT for the period (a) 01.06.2020 (b) 02.06.2020 (c) 03.06.2020 and (d) 04.06.2020 over IFR1, MELI, OUCA and TETN GNSS receiver stations.*

3.3.2. Variations of VTEC Against UT Between 5th and 8th June 2020 over IFR1, MELI, OUCA and TETN

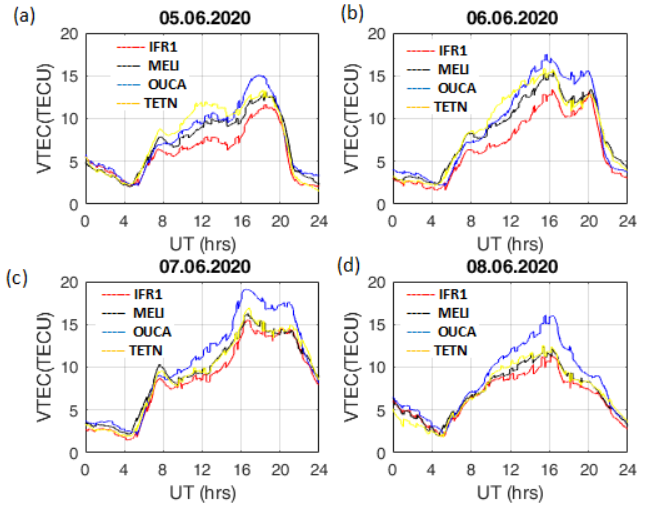

Figure 8. *Plot of VTEC against UT for period (a) 05.06.20200 (b) 06.06.2020 (c) 07.06.2020 and 08.06.2020 over IFR1, MELI, OUCA and TETN.*

Figure 8(a), 8(b), 8(c) and 8(d) shows VTEC against UT plots over IFR1, MELI, OUCA and TETN on 5th, 6th, 7th and 8th June 2020 respectively. Daily maximum VTEC values over all the four GNSS receiver stations were seen to rise between 5th and 7th June and drop on 8th June 2020. IFR1 had a daily maximum VTEC value of 11 TECU on 5th June, which rose to 13 TECU on 6th, 15 TECU on 7th June 2020 and dropped to 11 TECU on 8th June 2020. MELI had a daily maximum VTEC value of 13 TECU on 5th June, which increased to 15 TECU on 6th June, 16 TECU on 7th and reduced to 12 TECU on 8th June 2020. OUCA had a daily maximum VTEC value of 15 TECU on 5th June, which increased to 17 TECU on 6th June, 19 TECU on 7th June and dropped to 16 TECU on 8th June 2020. TETN had a daily maximum VTEC value of 13 TECU on 5th June, which increased to 16 TECU on 6th June, 17 TECU on 7th June and dropped to 12 TECU on 8th June 2020. Multiple TEC depletions of depths between 3 – 4 TECU were also observed over IFR1, OUCA, MELI and TETN on 5th, 6th and 7th June 2020.

3.3.3. Variations of VTEC Against UT Between 9th and 12th June 2020 over IFR1, MELI, OUCA and TETN

Figure 9(a), 9(b), 9(c) and 9(d) shows VTEC against UT plots over IFR1, MELI, OUCA and TETN on 9th, 10th, 11th and 12th June 2020 respectively. Daily maximum VTEC values over all the four GNSS receiver stations were seen to vary within a range of 13 to 16 TECU between 8th and 12th June 2020. IFR1 had a daily maximum VTEC value of 13 TECU on 9th, 10th and 12 June and 14 TECU on 11th June 2020. MELI had a daily maximum VTEC value of 14 TECU on 9th and 11th June 2020 and 14 TECU on 10th and 12th June 2020. OUCA had a daily maximum VTEC value of 15 TECU on 9th June, 16 TECU on 10th June, 17 TECU on 11th June and 18 TECU on 12th June 2020. TETN had a daily maximum VTEC value of 13 TECU on 9th June, 16 TECU on 10th and 11th June 2020 and 13 TECU on 12th June 2020. TEC depletions of depths of 5 TECU were observed over TETN on 9th, 10th, 11th and 12th June 2020.

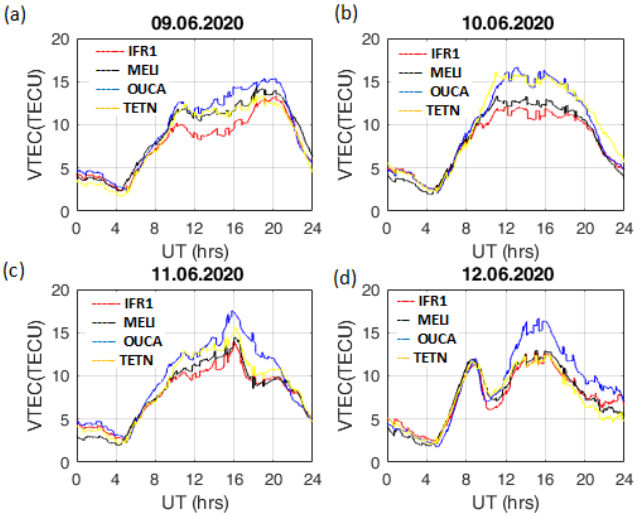

Figure 9. *Plot of VTEC against UT for period (a) 09.06.2020 (b) 10.06.2020 (c) 11.06.2020 and (d) 12.06.2020 over IFR1, MELI, OUCA and TETN.*

3.3.4. Variations of VTEC Against UT Between 13th and 16th June 2020 over IFR1, MELI, OUCA and TETN

Figure 10(a), 10(b), 10(c) and 10(d) shows VTEC against

UT plots over IFR1, MELI, OUCA and TETN on 13th, 14th, 15th and 16th June 2020 respectively. Daily maximum VTEC values over IFR1 were seen to vary within a range of 12 to 15 TECU between 13th and 16th June 2020. IFR1 had a daily maximum VTEC value varying between 10 and 15 TECU between 13th and 16th June 2020. MELI had a daily maximum VTEC value ranging between 10 TECU and 15 TECU between 13th and 16th June 2020. OUCA had a daily maximum VTEC value of between 13 TECU and 13 TECU between 13th and 16th June 2020. TETN had a daily maximum VTEC value of between 14 TECU and 16 TECU between 13th and 16th June 2020. TEC depletions of depths of 5 TECU were observed over TETN on 9th, 10th, 11th and 12th June 2020. It was however noted from Figure 10(a), 10(b) and 10(c) that the ionosphere over all the four GNSS stations was very disturbed between 12:00 UT and 20:00 UT on 13th, 14th, and 15th. Figure 10(d) shows the ionosphere over all the four GNSS stations disturbed the whole day on 16th June 2020.

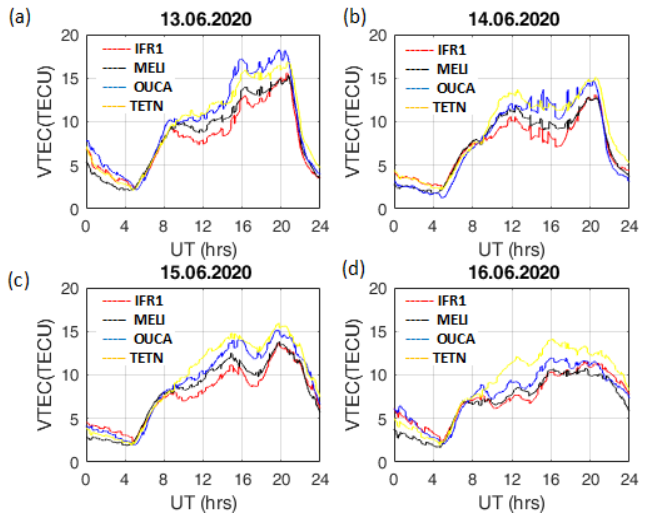

Figure 10. *Plot of VTEC against UT for period (a) 13.06.2020 (b) 14.06.2020, (c) 15.06.2020 and (d) 16.06.2020 over IFR1, MELI, OUCA and TETN.*

3.3.5. Variations of VTEC Against UT Between 17th and 20th June 2020 over IFR1, MELI, OUCA and TETN

Figure 11(a), 11(b), 11(c) and 11(d) shows VTEC against UT plots over IFR1, MELI, OUCA and TETN on 17th, 18th, 19th and 20th June 2020 respectively. Daily maximum VTEC values over the four GNSS stations appeared to fluctuate from day to day and station to station. IFR1 had a daily maximum VTEC value of 16 TECU on 17th June, 15 TECU on 18th June, 14 TECU on 19th June and 15 TECU on 20th June 2020. MELI had a daily maximum VTEC value of 16 TECU on 17th and 18th June, 15 TECU on 19th June and 18 TECU on 20th June 2020. OUCA had a daily maximum VTEC value of 18 TECU on 17th June, 20 TECU on 18th June, 16 TECU on 19th and 20th June 2020. MELI had a daily maximum VTEC value of 18 TECU on 17th and 18th June 2020, 16 TECU on 19th June and 20th June 2020. Multiple TEC depletions of depth between 3 to 6 TECU were also observed over IFR1, MELI, OUCA and MELI on 17th to 20th June 2020. The ionosphere over the four GNSS receiver stations also showed disturbances in all the days as indicated in Figures 11(a), 11(b), 11(c) and 11(d).

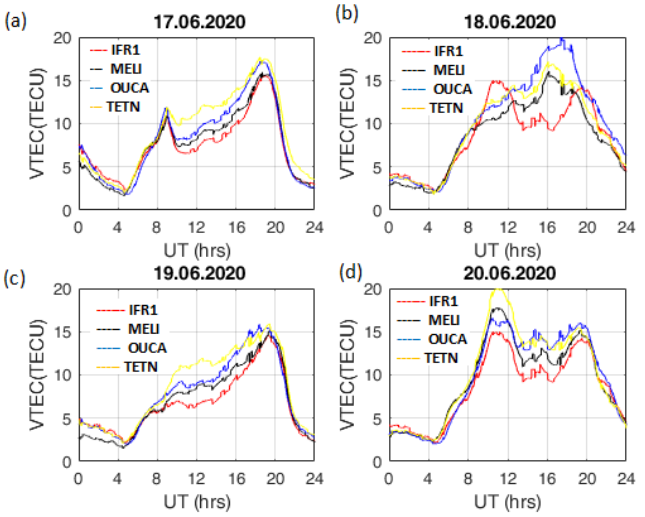

Figure 11. *Plot of VTEC against UT for period (a) 17.06.2020 (b) 18.06.2020 (c) 19.06.2020 and (d) 20.06.2020 over IFR1, MELI, OUCA and TETN.*

3.3.6. Variations of VTEC Against UT Between 21st and 24th June 2020 over IFR1, MELI, OUCA and TETN

Figure 12(a), 12(b), 12(c) and 12(d) shows VTEC against UT plots over IFR1, MELI, OUCA and TETN on 21st, 22nd, 23rd and 24th June 2020 respectively. Daily maximum VTEC values over the four GNSS receiver stations varied between 13 TECU and 16 TECU. IFR1 had a daily maximum VTEC value of 13 TECU on 21st and 24th June, 14 TECU on 22nd June and 12 TECU on 23rd June 2020. MELI had a daily maximum VTEC value of 13 TECU on 21st and 23rd June, 15 TECU on 22nd June and 14 TECU on 24th June 2020. OUCA had daily maximum VTEC values of 15 TECU on 21st and 24th June 2020, 16 TECU on 22nd and 23rd June 2020. MELI had a daily maximum VTEC value of 14 TECU on 21st, 22nd and 24th June 2020 and 13 TECU on 23rd June 22020. TEC depletions of depths 2 to 3 TECU were also observed. The ionosphere was also observed to be disturbed indicated by Figure 12(a), 12(b), 12(c) and 12(d).

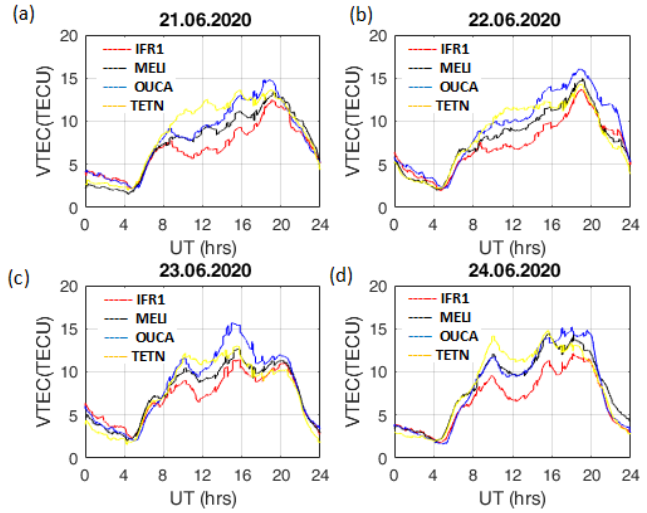

Figure 12. *Plot of VTEC against UT for period (a) 21.06.2020 (b) 22.06.2020 (c) 23.06.2020 and (d) 24.06.2020 over IFR1, MELI, OUCA and TETN.*

3.3.7. Variations of VTEC Against UT Between 25th and 28th June 2020 over IFR1, MELI, OUCA and TETN

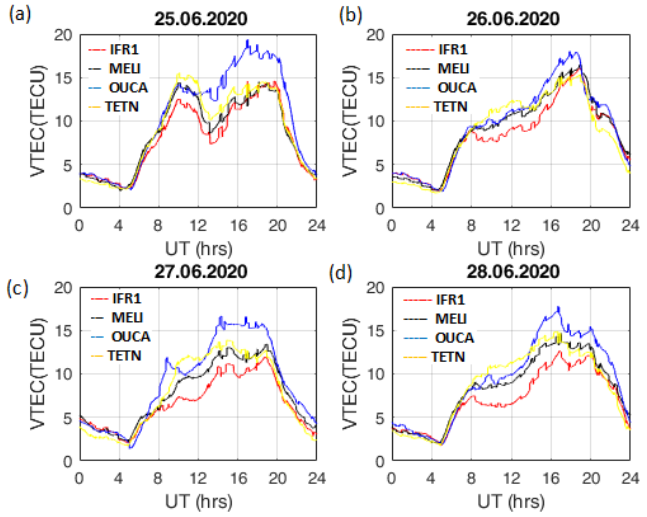

Figure 13. *Plot of VTEC against UT for period (a) 25.06.2020 (b) 26.06.2020 (c) 27.06.2020 and (d) 28.06.2020 over IFR1, MELI, OUCA and TETN.*

Figure 13(a), 13(b), 13(c) and 13(d) shows VTEC against UT plots over IFR1, MELI, OUCA and TETN on 25th, 26th, 27th and 28th June 2020 respectively. Large TEC depletions of depths 5 to 6 TECU were observed over the four GNSS receiver stations on 24th June 2020. However, smaller TEC depletions of depth 2- 3 TECU were also observed over IFR1 on 26th and 28th June and OUCA on 27th June 2020.

4. Discussions

4.1. Daily Ionospheric TEC Variability over IFR1, MELI, OUCA and TETN During the Godzilla SDS Event of June 2020

We have investigated the possible relation between ionospheric TEC perturbations and the Godzilla SDS event of June 2020 over Morocco. In Figures 2, 3, 4 and 5, the aerosol concentrations levels over OUCA, IFR1, TETN and MELI resulting from the Godzilla SDS kept varying between 1st June and 28th June 2020. Between 1st and 4th June there were very low aerosol concentrations over the four GNSS receiver stations. Between 5th and 13th June, the aerosol concentrations over OUCA were seen to increase steadily but MELI, IFR1 and TETN still experienced low aerosol concentrations. From 14th to 18th June 2020, OUCA experienced increased aerosol concentrations. On 19th June 2020, MELI and OUCA experienced high aerosol concentrations. Between 20th and 22nd June 2020, OUCA continued to experience higher aerosol concentration levels. Between 23rd and 26th June 2020, all the four GNSS receiver stations experienced increased aerosol concentrations. These changes in the aerosol levels over the four GNSS receiver stations could directly be linked to the variability of VTEC against UT between 1st and 28th June as indicated by Figures 7, 8, 9, 10, 11, 12 and 13. It is noted that between 1st and 11th June 2020, there were very minimal ionospheric TEC perturbations as depicted by the VTEC plots in Figures 7, 8 and 9. Between 12th and 18th June 2020, visible ionospheric TEC perturbations were noted over all the GNSS receiver stations and corresponded to increased aerosol concentrations in the atmosphere. Between 19th and 26th June 2020, there were increased ionospheric TEC perturbations over all the four GNSS receiver stations. It should be noted that all the four GNSS receiver stations exhibited these ionospheric TEC disturbances. This is because during SDS events, sand and dust particles are blown up above the ground and once they are suspended, they are advected thousands of kilometers from their point of origin and hence the generated electric fields propagate horizontally over considerable distances ending up affecting electron density thousands of kilometers away [39]. Since June 2020 is a geomagnetically quiet period as depicted by the solar wind parameters and geomagnetic indices in Figure 6 [40], the observed variability of the ionosphere above the four GNSS receiver stations in Morocco can only be attributed to two possible ionization sources. One of the sources is the presence of the Extreme Ultra Violet (EUV) radiation from the Sun, which varies over a 24 hour period between daytime and nighttime and over a 11 year period within solar cycle. The diurnal variation of VTEC with time over IFR1, MELI, OUCA and TETN for most days shows characteristics typical to low latitude ionosphere where VTEC is low during pre-dawn, then increases gradually reaching maximum in the afternoon and then gradually decreasing after sunset [41, 42]. The other possible source of

ionospheric TEC variability during the SDS event is the atmospheric electrification resulting from the fast moving sand and dust particles in the atmosphere. Atmospheric transport, suspension and interaction of individual sand and dust particles rapidly bring up a substantial amount of electrification [11]. Extensive flow-based modeling has shown that rotating dust systems (dust devils) can produce very large electric fields in excess of 10kV/m within few seconds [11, 43, 44]. The dust electrification process during sand and dust storm events is due to contact and triboelectric charging between blowing sand and dust particles. Duf, N. f & Lacks, D. J. suggested that during collisions, the smaller sand and dust particles acquire negative charge with respect to larger particles. The larger particles usually stay close to the surface while charged smaller particles are brought into suspension and transported into the atmosphere by local turbulence. This gravitational charge separation is always consistent with increase in atmospheric electric fields [45]. The charge separation maintains current flow between the lower atmosphere and the ionosphere through a Global Electric Circuit (GEC) model [11]. The ionosphere responds to the generated atmospheric electric field by modifying the ionospheric conductivity. Electrical conductivity which is the ratio between current density (i in A/m) and electric field (E in V/m) is given by equation 6 [15],

Electrical conductivity,

$$\sigma = {i}/{E} = {Nev}/{E} \tag{6}$$

Where v is the velocity of the relevant particles, N is their concentration and *e* is the charge on each.

The horizontal layering of the ionosphere has the greatest effect on vertical currents. This affects the rate at which ions and electrons recombine, hence producing both positive phases (exhibited as increases in electron concentration) and negative phases (exhibited as decreases in electron concentration) in the ionosphere [15, 46] as observed in the VTEC plots in Figures 7, 8, 9, 10, 11, 12 and 13.

By tracking the movement of the Godzilla SDS as indicated in Figures 2, 3, 4 and 5, it was noted that the intensity of the storm over Morocco was higher between 16th and 26th June 2020. The dust plume was therefore considered to have been so much electrically active during this period. This corresponded with increased ionospheric TEC disturbances recorded on 16th, 17th, 18th, 20th, 21st, 22nd, 23rd, 24th and 25th June 2020. These results conform with results from earlier studies done by [14, 20] on possible relations between sand and dust storm and ionospheric TEC perturbations.

4.2. Variations of Daily Maximum VTEC Values During the Godzilla SDS of June 2020 over IFR1, MELI, TETN and OUCA

The variations of daily maximum VTEC values for each day from 1st to 28th June 2020 and for each station were plotted in a scatter plot as in Figure 14. Across all the four GNSS receiver stations, continuous increases and decreases of daily maximum VTEC values were observed from 1st to 28th June 2020. Since this behavior is occurring during days having low aerosol concentrations and those having high aerosol concentrations in the atmosphere, this might not be directly linked to the effect of the Godzilla SDS event. However, we might link it to the extra Earth warming which degenerated into extreme convectional currents, which was a precursor for the Godzilla SDS [6] and was propagated further during the SDS event due to change in atmospheric composition brought about by the change in global circulation pattern of the charge structures. The global circulation pattern majorly depends on the variation in particle charge with particle size and the effect of gravitational charge separation [11]. The VTEC plots for each day over all the for receiver stations exhibited similar trends. This shows that they exhibited almost similar ionospheric dynamics.

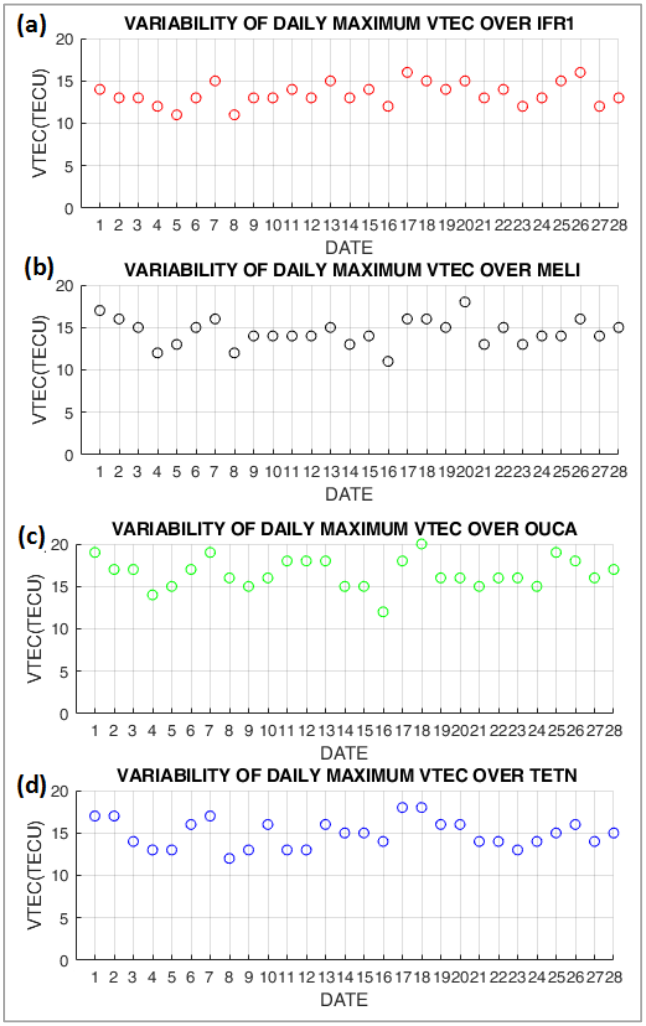

Figure 14. *Scatter plots showing variability of daily maximum VTEC values over (a) IFR1, (b) MELI, (c) OUCA and (d) TETN between 1st and 28th June 2020.*

4.3. VTEC Depletions and Nighttime VTEC Enhancements During the Godzilla SDS of June 2020 over IFR1, MELI, OUCA and TETN

In this study, VTEC depletions of depths 3 to 6 TECU over all the four GNSS receiver stations were noted on 12th, 14th, 17th, 20th and 25th June 2020. Successive TEC depletions were also noted over the four GNSS receiver stations on 16th and 23rd June 2020. However, some days had VTEC depletions and enhancements occurring at around 20:00 UT. These enhancements occurred after the Pre-reversal enhancement (PRE) and thus regarded as nighttime VTEC enhancements. Their occurrences were summarized in Table 2 as shown.

Table 2. *Nighttime peak of VTEC for IFR1, MELI, OUCA and TETN between 1st and 28th June 2020.*

DATE	GNSS Receiver Station	Occurrence Time
9th June 2020	IFR1, OUCA, MELI, TETN	20:00 UT
13th June 2020	IFR1, OUCA, MELI, TETN	21:00 UT
15th June 2020	IFR1, OUCA, MELI, TETN	20:00 UT
17th June 2020	IFR1, OUCA, MELI, TETN	20:00 UT
19th June 2020	IFR1, OUCA, MELI, TETN	20:00 UT
20th June 2020	IFR1, OUCA, MELI, TETN	20:00 UT
21st June 2020	IFR1, OUCA, MELI, TETN	20:00 UT

In Table 2, it is clearly noted that nighttime VTEC enhancements majorly occurred between 20:00 and 21:00 UT on 9th, 13th, 15th, 17th, 19th, 20th and 21st June 2020 over all the four GNSS receiver stations. It is also noted that this is the period when the intensity of the Godzilla SDS began increasing over Morocco and hence there seemed to be a relationship between the SDS event and the occurrence of nighttime VTEC enhancements. Although previous studies on VTEC have observed increases in nighttime VTEC enhancements, there is still no agreement on their origin [47]. However, some studies suggest that the nighttime VTEC enhancements might be associated with the westward directed electric field [47, 48]. In fair weather environment, the ionosphere and protonosphere are strongly coupled through the charge exchange reactions between protons and atomic oxygen ions. That is, as the F-region builds up after sunrise, plasma moves up to higher latitudes where protons are created and flow up along the field lines to populate the protonosphere. Proton population flows back to the lower levels in the evening, where it charge-exchanges back to oxygen ions, thus helping maintain the F-regions at night [15]. Modeling studies by Jackson, T. L. et al (a); Kok, J. F. & Renno, N. O. and Jackson, T. L. et al, (b) have shown that in the sand and dust environment, the electron avalanche processes which include dust and electron absorption or losses and the active conversion to electron dissociative attachment could develop after sunset leading to electron excitation and new chemical products [49-51]. Polarization charges arising from the conductivity gradients at the terminator enhances eastward electric field after sunset for more than an hour [52]. Farrel, W. M. et al noted that the electron avalanche represents a substantial modification of the atmospheric conductivity [53]. This modification might also be the cause of the occurrence of nighttime VTEC enhancements since the penetration of electrons and ions from the upper atmosphere into the ionosphere contributes to extraordinary production of electrons and ions in the ionosphere.

Although the study has revealed day to day ionospheric TEC variability during the Godzilla SDS event, questions about the physical mechanism responsible for some observed variability remains unanswered. For example, it still remains unclear how much of the observed variability is due to inherent variations in the atmosphere-ionosphere interactions and how much can be attributed to mesospheric processes.

5. Conclusion

In this paper, we have considered an interesting SDS event and used TEC measurement to bring out possible ionospheric TEC variability resulting from atmospheric-ionospheric interaction during the SDS storm event. Our results have shown increased electron density perturbations over the four GNSS receiver stations between 16th and 28th June 2020. The daily maximum VTEC values over the four GNSS receiver stations also showed an interesting trend of significant enhancement and decrease in the whole study period. The VTEC plots for each day over all the four GNSS receiver stations exhibited similar trends, hence exhibited similar ionospheric dynamics. VTEC depletion of depths 3 to 6 TECU over all the four GNSS receiver stations were noted on 12th, 14th, 17th, 20th and 25th June 2020. Nighttime VTEC enhancements were also noted to majorly occur between 20:00 and 21:00 UT on 9th, 13th, 15th, 17th, 19th, 20th and 21st June 2020. This might be attributed to the development of the electron avalanche processes including dust and electron absorption or losses and the active conversion to electron dissociative attachment leading to electron excitation. Electron avalanche has been known to represent a substantial modification of the atmospheric conductivity. Thus, energetic particles like electrons and ions from the upper atmosphere can penetrate the ionosphere and contribute to extraordinary production of electrons and ions in the ionosphere influencing electron density.

Abbreviations

ESA	European Space Agency
GEC	Global Electric Circuit
GEE	Google Earth Engine
GIM	Global Ionospheric Maps
GNSS	Global Navigation Satellite System
GPS	Global Positioning System
IEF	Interplanetary Electric Field
IMF	Interplanetary Magnetic Field
Kv	Kilo-Volt
Kv/m	Kilo-Volt Per Metre
MHz	Mega-Hertz
NOAA	National Oceanic and Atmospheric Administration
PPP	Precise Point Positioning
RINEX	Receiver Independent Exchange
RST	Robust Satellite Technology
SAI	Sentinel-5P Aerosol Index
SEVIRI	Spinning Enhanced Visible & Infrared Imager
SDS	Sand and Dust Storm
STEC	Slant Total Electron Content
TEC	Total Electron Content
TECU	Total Electron Content Unit
UT	Universal Time
USA	United States of America

Acknowledgments

The authors thank the University of NAVSTAR Consortium: http://unavco.org/data/gps-gnssdata/ for the GNSS data; Kyoto: *wdc.kugi.kyoto.u.ac.jp/dst/index.html* and Kyoto: *www.kugi.kyoto-ua.ac.jp/kp* for the geomagnetic activity data; *https://omniweb.gsfc.nasa.gov/form/dx1.html* for the daily values of solar wind parameters and the European Space Agency for the Copernicus Sentinel-5P satellite images of June 2020 Godzilla SDS over the Sahara. They also thank Prof Gopi Seemala of the Indian Institute of Geomagnetism for the GPS-TEC analysis software.

Author Contributions

Uluma Edward: Conceptualization, Data curation, methodology, data analysis, software, resources, writing and editing original document and revision of the final manuscript.

Chali Idosa Uga: Conceptualization, Data curation, methodology, data analysis, software, writing and editing original document and revision of the final manuscript.

Athwart Davis Odhiambo: Reviewing and Editing the original draft, software, methodology, data analysis and revision of the final manuscript.

Binod Adhikari: Reviewing and Editing the original draft, software, methodology, data analysis and revision of the final manuscript.

Sujan Prasad Gautam: Reviewing and Editing the original draft, software, methodology, data analysis and revision of the final manuscript.

Ndinya Boniface: Reviewing and Editing the original draft, software, methodology, data analysis and revision of the final manuscript.

Omondi George: Reviewing and Editing the original draft, software, methodology, data analysis and revision of the final manuscript.

Ashutosh Giri: Reviewing and Editing the original draft, software, methodology, data analysis and revision of the final manuscript.

Dessalegn Teferi: Reviewing and Editing the original draft, software, methodology, data analysis and revision of the final manuscript.

Negasa Belay: Reviewing and Editing the original draft, software, methodology, data analysis and revision of the final manuscript.

Ashok Silwal: Reviewing and Editing the original draft, software, methodology, data analysis and revision of the final manuscript.

Funding

This work did not receive any funding.

Data Availability Statement

Data can be made available on request.

Conflicts of Interest

The authors declare no conflicts of interest.

References

[1] WBO-Bulletin-2015. Airborne dust: A hazard to human health, environment and society, 2022, vol 64(2).

[2] Borunda, A. Saharan dust is bad for health. But it is also crucial to Earths biology and climate. National geographic, 2020.

[3] Yu, H., Chin, M., Yuan, T. L., Bian, H., Remer, L. A., Prospero, J. M., Omar, A, et al., The fertilizing role of the African dust in the Amazon rainforest: A first multi-Year assessment based on CALIPSO lidar observations. Geophys. Res. Lett., 42, 2015, 1984-1991, https://doi.org/10.1002/2015GLO63040

[4] Remini, B. The Sahara: A wind dynamics on surface and water in depth. Larhyss Journal 47(2021), 189-207, https://larhyss.net/ojs.index.php/larhyss/index

[5] Zhongming, Z., Linong, L., Xiaona, Y., Wangqiang, Z., Wei, L. Satellites and Unusual Sahara dust plume, 2020.

[6] Asare-Ansah, A. B., Twumasi, Y. A., Ning, Z. H., Ansah, P. B., Frimpong, D. B., Owusu, F., Apraku, C. Y., Anokye, M., Loh, M., Armah, R. D. N., Opong, J. Tracking the Godzilla Dust plume using the Google Earth Engine Platform. The international Archives of the photogrammetry, Remote sensing and spatial information sciences, Vol. XLVI-M-2-2022, ASPRS 2022 Annual conference, 6-8 February and 21-25 March 2022, Denver, Colorado, USA and Virtual. https://doi.org/10.5194/isprs-Archives-XLVI-M-2-2022-33-2022

[7] Zhao, B., Wan, W., Lie, L., et al. Features of annual and semi-annual variations derived from the global ionospheric of total electron content. Annales Geophysicae, Copernicus GmbH 2007, pg 2513-2527.

[8] Gundala, S. S., Jakkampudi, C. S., Yadavalli, A., (2021). Ionospheric total electron content and scintillations characteristics from GPS signal observations at a low latitude station, (2021, Materials today: Proceedings.

[9] Rukundo, W., Shiokawa, K., Alsaid, A., et al. A machine learning approach for total electron content (TEC) prediction over the northern anomaly crest in Egypt, 2022. Advances in space Research.

[10] Shim, J. A. S. Analysis of total electron content (TEC) variation over low-middle Latitude ionosphere. PhD thesis, 2009, Uta University. Paper 403.

[11] Harrison, R. G., Barth, E., Esposito, F., Merrison, J., Montmessin, F., Aplin, K. L., Borlina, C., Berthelier, J. J., Deprez, G., Farrell, W. M., Houghton, S. N., Zimmerman, M. Applications of electrified dust and dust device electrodynamics to Martian Atmospheric electricity. Space scipex, 2016, 203: 299-345. https://doi.org/10.1007/s11214-016-0241-8

[12] Pulinets, S., Ouzoinov, D. The possibility of earthquake forecasting. Learning from nature. IOP publishing, 2018, Bristol pg. 167.

[13] Pulinets, S., Davidenko, D. Ionospheric precursors of earthquakes and Global Electric Circuit. Adv. In space Res. 53, 2014, 709-723. https://doi.org/10.1016/j.asr.2013.12.035

[14] Pulinets, S., Davidenko, D. and Pulinets, M. Atmosphere – ionosphere coupling induced by volcano eruptions and dust storms and role of GEC as the agent of geopsheres interaction. Advances in space research, 2022, https://doi.org/10.1016/j.asr.2022.03.031,4319-4334

[15] Hargreaves, J. K. The solar-terrestrial environment, Cambridge Atmospheric and Space Sciences series, 1992, Cambridge Univ. Press, Cambridge, UK.

[16] Hoppel, W. A., Anderson, J. C. W. Atmospheric electricity in the planetary boundary layer. In: The Earth's Electrical Environment. National Academic Press, Washington, DC, 1986, pp. 149–165.

[17] Gringel, W., Rosen, J. M. and Hofmann, D. J. Electrical structure from 0 to 30 km atmospheric electricity in the planetary boundary layer: The Earth's electrical environment; National Academic press: Washington DC, USA, 1986, PP 166-182.

[18] Pulinets, S. A., Boyarchuk, K. A., Khagai, V. V., Kim, V. P. and Lomonosov, A. M. Quasi-electrostatic model of the atmosphere-thermosphere-ionosphere coupling. Adv Space Res. 2000, 26, 1209-1218.

[19] Ulanowski, Z., Bailey, J., Lucas, P. W., Hough, J. H. and Hirst, E. Alignment of Atmospheric mineral dust due to electric field. Atmos. Chem. Phys. 7, 2007, 6161-6173.

[20] Tramutoli, V., Marchese, F., Falconieri, A., Fillizola, C., Genzano, N., Hattori, K., Lisi, M., Liu, J., Ouzounov, D., Parrot, M., Pergola, N. and Pulinets, S. Tropospheric and ionospheric anomalies induced by volcanic and Sahara Dust events as part of the geosphere interaction phenomena. Geosciences 2019, 9, 177, https://doi.org/10.3390/geosciences9040177

[21] Seemala, G. and Valadare, C. Statistics of total electron content depletions observed over the South American continent for the year 2008, Radio Science, 2011, vol. 46. Gurtner, W., Estey, L. (2007) Rinex-the receiver independent exchange format-version 3.00. Astronomical Institute, University of Bern and UNAVCO, Bolulder, Colorado.

[22] Gurtner W., Estey, L. RINEX the receiver independent exchange format-version 3.00. Astronomical institute, University of Bern and UNAVCO, Bolulder, Colorado, 2007.

[23] Tariku YA. Patterns of gps-tec variation over low-latitude regions (African sector) during the deep solar minimum (2008 to 2009) and solar maximum (2012 to 2013) phases. Earth, Planets and Space, 2015, 67(1): 1–9.

[24] Horvath I, Crozier S. Software developed for obtaining GPS-derived total electron content values. Radio Science, 2007, 42(02): 1–20.

[25] Cepni MS, Potts LV, Miima JB. High-resolution station-based diurnal ionospheric total electron content (TEC) from dual-frequency GPS observations. SpaceWeather, 2013, 11(9): 520–528.

[26] Ma X, Maruyama T, Ma G, et al. Three-dimensional ionospheric tomography using observation data of GPS ground receivers and ionosonde by neural network. Journal of Geophysical Research: Space Physics, 2005, 110(A5).

[27] Jin, S., Park, J., Wang, J., Choi, B. and Park, P. Electron density profiles derived from Ground-based observations. The Journal of Navigation, 2006, 59(3): 395-401.

[28] Heise S, Jakowski N, Wehrenpfennig A, et al. Sounding of the topside ionosphere/ plasmasphere based on GPS measurements from champ: Initial results. Geophysical Research Letters, 2002, 29(14): 44–1.

[29] Jawoski, N., Mayer, C., Hoque, M. and Wilken, V. Total electron content models and their use in ionosphere monitoring. Radio science, 2011, 46(06): 1-11.

[30] Ciraolo, L., Azpilicueta, F., Brunini, C., Meza, A. and Radicella, S. M. Calibration errors on experimental slant total electron content determined by the GPS. Journal of Geodesy, 2007, 81: 111-120.

[31] Kassa T, Damtie B. Ionospheric irregularities over Bahir dar, Ethiopia during selected geomagnetic storms. Advances in Space Research, 2017, 60 (1): 121–129.

[32] Otsuka, Y., Ogawa, T., Saito, A., Tsugawa, T., Fukao, S., Miyazaki, S. A new Technique for mapping of total electron content using GPS network in Japan. Earth, Planets and space. 2002, 54(1): 63-70.

[33] Sardon, E. and Zarraoa, N. Estimation of total electron using GPS data: How stable are the differential satellite and receiver instrumental biases? Radio science, 1997, vol. 32, No. 5, pp. 1899-1910.

[34] Gorelick, N., Hancher, M., Dixon, M., Ilyushchenko, S., Thau, D., Moore, R. (2017). Google Earth Engine: Planetary-scale geospatial analysis for everyone. Remote sensing and Environment, 2017, 202, 18-27.

[35] De Graaf, M., Stammes, P., Torres, O., Koelemeijer, R. B. A. Absorbing Aerosol Index: Sensitivity analysis, application to GOME, and comparison to TOMS. Journal of Geophysical Research: Atmospheres, 2005, 110(D1).

[36] Jethva, H., Satheesh, S. K., Srinivasan, J. Seasonal variability of aerosols over the Indo-Gangetic basin. Journal of Geophysical Research: Atmospheres, 2005, 110(D21).

[37] Althaf, P., Shaeb, K. H. B., Kumar, K. R. Hotspot analysis and long-term trends of absorbing aerosol index from dust emissions were measured by the Ozone measuring Instrument at different Urban locations in India from 2005 to 2008. Atmospheric environment, 2022, 118933.

[38] Warren, C. Godzilla dust storm traced to shaky northern jet stream. Retrieved May 2023, from science: https://www.science.org/content/article/godzilla-dust-storm-Traced-shaky-northern-jet-stream,2022

[39] Grousset, F. E., Ginoux, P., Bory, A., Biscaye, P. E. Case study of a Chinese dust plume reaching the French Alps. Geophysical Research Letters, 2003, 30(6), 1277, https://doi.org/10.1029/2002GL016833

[40] Kamide, Y. and Chian, A. Hand Book of the Solar-Terrestrial environment. Springer Berlin Heidelberg, New York. 2007, ISBN 978-3-540-46314-6. https://doi.org/10.007/6104478

[41] Bagiya, S. Mala, Joshi, H. P., Iyer, K. N., Aggarwal, M., Ravindran, S., & Pathan, B. M. TEC variations during low solar activity period (2005-2007) near the Equatorial Ionospheric Anomaly Crest Region in India. *Annales Geophysicae, 2009, 27*, pp. 1047-1057.

[42] Fayose, R. S., Oladosu O. R., Rabius A. B. and Grooves. Variation of Total Electron Content [TEC] and Their Effect on GNSS over Akure, Nigeria. http://dx.doi.org/10.5539/apr.v4n2p105,2012

[43] Jackson, W. M. Farrell. Electrostatic fields in dust devils: an analog to Mars. IEEE Trans. Geosci. RemoteSens. 2006, 44(10), 2942–2949. https://doi.org/10.1109/TGRS.2006.875785

[44] Williams, E., Nathou, N., Hicks, E., Pontikis, C., Russel, B., Miller, M., Bartholomew, M. J. The electrification of dust-lofting gust fronts ('haboobs') the Sahel. Atmos. Res. 2009, 91, 292–298.

[45] Duff, N., Lacks, D. J. Particle dynamics simulations of triboelectric charging in granular insulator systems. J. Electrost. 2008, 66, 51. https://doi.org/10.1016/j.elstat.2007.08.005

[46] Kelley, Michael C. The Earth's Ionosphere: Plasma Physics and Electrodynamics, 1998, Academic Press.

[47] Horvath, I., and Essex, E. A. Investigating the mid-latitude nighttime TEC enhancements their relation to the low-latitude ionosphere and at low sunspot numbers, in: Workshop on the Applications of Radios Science, 2000, http://www.sws.bom.gov.au/IPSHosted/NCRS/wars/wars2000/commg/horvath.pdf

[48] Chen, Y., Ma, G., Huang, W., Shen, H., & Li, J. Night-time total electron content enhancements at equatorial anomaly region in China. Advances in Space Research, 2008, 41(4), 617-623.

[49] Jackson, T. L., Farrell, W. M., Delory, G. T., Nithianandam, J. Effect of dust absorption on the electron avalanche process occurring within Martian dust storms. Geophys. Res. Lett., 2008, 35, L1620. https://doi.org/10.1029/2008GL034523

[50] Kok, J. F., Renno, N. O. Electrification of wind-blown sand on Mars and its implications for atmospheric chemistry. Geophys. Res. Lett., 2009, 36, L05202. https://doi.org/10.1029/2008GL036691

[51] Jackson T. L. et al. Martian dust devil electron avalanche process and associated electrochemistry. J. Geophys. Res., 2010, 115, E05006 (2010).

[52] Seemala Seemala, G. K. & Valladares, C. E. Statistics of total electron content depletions observed over the South American continent for the year 2008. Radio Sci., 2008, 46, RS5019, https://doi.org/10.1029/2011RS004722

[53] Farrell, W. M., McLain, J. L., Collier, M. R., Keller, J. W., Jackson, T. J., Delory, G. T. Is the electron avalanche process in a Martian dust devil self-quenching? Icarus, 2015, 254, 333–337.